Published in final edited form as:
Magn Reson Imaging. 2008 June ; 26(5): 703–714. doi:10.1016/j.mri.2007.11.001.

Concurrent correction of geometric distortion and motion using the map-slice-to-volume method in EPI

Desmond T. B. Yeo[a,b], **Jeffrey A. Fessler**[a,b], and **Boklye Kim**[a,*]

[a]Department of Radiology, University of Michigan Medical School, Ann Arbor, Michigan 48109, USA.

[b]Department of Electrical Engineering and Computer Science, University of Michigan, Ann Arbor, Michigan 48109, USA.

Abstract

The accuracy of measuring voxel intensity changes between stimulus and rest images in fMRI echo-planar imaging (EPI) data is severely degraded in the presence of head motion. In addition, EPI is sensitive to susceptibility-induced geometric distortions. Head motion causes image shifts and associated field map changes that induce different geometric distortion at different time points. Conventionally, geometric distortion is "corrected" with a static field map independently of image registration. That approach ignores *all* field map changes induced by head motion. This work evaluates the improved motion correction capability of mapping slice to volume (MSV) registration with concurrent iterative field corrected reconstruction using updated field maps derived from an initial static field map that has been spatially transformed and resampled. It accounts for motion-induced field map changes for translational and in-plane rotation motion. The results from simulated EPI time series data, in which motion, image intensity and activation ground truths are available, show improved accuracy in image registration, field corrected image reconstruction and activation detection.

Keywords

Field-inhomogeneity; fMRI; Motion correction; Geometric distortion; Activation detection

1. Introduction

In functional MRI (fMRI) studies, activation maps are generated by statistical analyses of voxel intensity changes between stimulus and rest images of echo-planar imaging (EPI) time series data. The accuracy of measuring these intensity changes, which are typically in the

*Corresponding author. Basic Radiological Sciences Division, Department of Radiology, University of Michigan Medical School, 109 Zina Pitcher Place, AC51 BSRB, MI 48109-2200, USA. Tel.: +1-734-763-5692; Fax: +1-734-615-1471. boklyek@umich.edu (Boklye Kim).

range of 1% to 4%, is severely degraded in the presence of head motion. To compensate for head motion, some studies employ in-plane and volumetric image registration techniques on EPI time series data [1-4]. Single-shot EPI data is also sensitive to magnetic susceptibility(χ)-induced geometric distortions, especially for the mid to lower brain regions near air-tissue and bone-tissue interfaces. Subject motion causes image shifts as well as field-map changes which result in time-varying local changes in geometric distortion [5,6]. Consequently, inconsistencies in voxel positions across the time series images degrade statistical testing of the signal changes in response to the given tasks in activation studies.

In fMRI, geometric distortion correction typically is performed with a static field-map independently of motion correction [6,7], thus ignoring field-map changes caused by head motion. A prospective approach to this problem is to acquire field-maps simultaneously with EPI data during an fMRI experiment to track temporal field-inhomogeneity changes by collecting additional *k*-space data [8,9]. However, acquisition of extra *k*-space data within reasonable time may pose some limitations in field-map resolution since, to reduce scan time, the extra data acquired is typically constrained to a low-pass filtered or truncated version of a full set of EPI image *k*-space data. Also, modifying pulse sequences may not be an available option in many clinical scanners. In addition, some of the algorithms for image reconstruction and post-processing are computationally intensive [9]. A correction strategy [10] based on the work done by Chang and Fitzpatrick [11] is of notable interest since no field-maps are required a priori. Instead, pairs of EPI images are acquired with opposing blipped phase encode gradient polarity, thus yielding image pairs with identical geometric distortion but in opposite directions along the phase encoding axis. The deformation field between each pair of images, from which the dynamic field-map is computed, is estimated from the images' intensity values. However, to acquire the pairs of EPI images, pulse sequence modification is required, and motion-induced field-map changes may occur between the acquisitions. This may lead to local differences in geometric distortion in each pair of images, especially in regions with susceptibility-induced field-inhomogeneity, which may yield inaccurate field-map estimates. Another retrospective correction method [5] adopts a least squares approach and models the temporal change in B_0 using a Taylor series expansion with respect to motion parameters. Qualitative results indicate good correlation between estimated and measured parameters. This model was designed for registration and geometric distortion correction of mono-modality EPI time series images with a preselected EPI volume as a reference volume. An anatomically correct structural volume was not used for registration.

Previously, in our group, a realistic motion-correction approach by mapping a slice-to-volume (MSV) for multi-slice EPI time series was developed [12]. This technique, which uses negated mutual information as the similarity cost metric, allows individual slices in the time series to be mapped to an anatomically correct reference volume, and can accurately correct image shifts due to 3D rigid head motion. Compared to the widely used volumetric registration of EPI volumes, which ignore inter-slice motion, the MSV approach improved sensitivity and specificity in localizing activated regions [12]. Moreover, receiver operating curve (ROC) analyses of detected activation from MSV-corrected simulated datasets and datasets processed by SPM suggest that MSV improves activation detection results [13].

Although rigid-body transformations may suffice for activation localization in the sensorimotor cortex, geometric distortions in conventionally reconstructed EPI slices acquired from the mid to lower brain regions cause difficulty in localizing activations, which makes language studies with fMRI difficult. Consequently, MSV was expanded to include a non-linear warping function for studies involving mid brain regions [14,15]. This improvement increases computation due to the longer optimization process associated with higher degrees of freedom in registration.

This work evaluates an extension of MSV with concurrent field-inhomogeneity correction for EPI time series images and was introduced previously using a small test dataset with known motion parameters [16]. The concurrent field-map MSV (CFMMSV) method employs iterative field-corrected quadratic penalized least squares (QPLS) image reconstruction [17] followed by a field-map update to enhance the MSV rigid body motion-correction scheme, therefore accounting for field-inhomogeneity changes with inter-slice head motion. The proposed method consists of iterative correction cycles, each with a pair of QPLS image reconstruction and MSV motion correction stages. In each cycle, dynamic field-map slices are re-sampled from a high resolution 3D static field-map that has been spatially transformed by a rigid body transformation function determined by MSV for the respective EPI slices. Since geometric distortion is corrected incrementally in the QPLS stage after each field-map update, a rigid body MSV motion model should suffice and requires less computation than non-linear MSV registration. For two sets of realistically simulated EPI time series with different ground truths for rigid body motion, image intensities and activation regions, results show that the CFMMSV method improves the accuracy of the estimated motion parameters and reconstructed images when compared to a strategy that performs geometric distortion and motion correction independently using just a static field-map. Non-parametric random permutation tests were also performed on all datasets at various stages in the CFMMSV correction process to compute activation detection (ROC) curves. The areas under these ROC curves show that the CFMMSV method improves the activation detection accuracy.

2. Background

2.1 EPI Geometric Distortion

In brain EPI data that is reconstructed without field-inhomogeneity correction, geometric distortion is observed in regions where the local magnetic field is inhomogeneous, especially at the boundaries of tissues with significant magnetic susceptibility differences. Head motion that changes the orientation of the inter-tissue boundary with B_0 (out-of-plane rotations) may induce significant field-inhomogeneity changes in the region around the boundary. The effects of this type of motion, which include two out-of-plane rotations, are not modeled in this work. Translations and in-plane rotation are less likely to cause such local changes in the susceptibility-induced component of the field-map, and mainly induces shifts and in-plane rotation of the entire field-map. In EPI, due to the long readout time, field-inhomogeneity causes pixel shifts, mainly in the phase encoding direction [18,19]. These shifts depend on the EPI slice readout time *Treadout* and the point field-inhomogeneity $\Delta B(x_i,y_j)$. The space-variant pixel shift in the phase encoding direction

causes geometric distortion and intensity accumulation or spread, which adversely affect fMRI activation detection.

2.2 Iterative Field-Corrected Reconstruction

To perform geometric distortion correction, we use an iterative field-corrected reconstruction method that, unlike many non-iterative image reconstruction methods, does not assume a smooth field-map [17]. The continuous object f and field-map $\Delta\omega_{\text{static}}$ are parameterized into a sum of weighted rect functions $\Phi(\boldsymbol{r}-\boldsymbol{r}_n)$ where $\boldsymbol{r}$ is the vector of spatial coordinates. Ignoring spin relaxation and assuming uniform receiver coil sensitivity, the observed MR raw data of slice frame l is

$$u^l(t_m) = s^l(t_m) + \varepsilon^l(t_m), \quad l = 0 \ldots L-1, \quad (1)$$

and the parameterized MR signal equation of slice l is

$$s^l(t_m) = \Phi(\mathbf{k}(t_m)) \sum_{n=0}^{N-1} f_n^l e^{-j\Delta\omega_n^l t_m} e^{-j2\pi(\mathbf{k}(t_m)\cdot\mathbf{r}_n)}, \quad l = 0, \ldots, L-1, \quad (2)$$

where $s^l(t_m)$ is the baseband MR signal sample at time t_m during readout, $\varepsilon^l(t_m)$ denotes white Gaussian noise [20], $\Phi(\boldsymbol{k}(t_m))$ denotes the Fourier transform of $\Phi(\boldsymbol{r})$, N is the number of pixels in a slice, L is the total number of slice frames in the EPI time series and f_n^l and $\Delta\omega_n^l$ are the object intensity and field-inhomogeneity values, respectively, at $\boldsymbol{r}_n$. The matrix-vector form of Eq. (1) can be written as follows:

$$\boldsymbol{u}^l = \boldsymbol{A}^l \boldsymbol{f}^l + \boldsymbol{\varepsilon}^l \quad (3)$$

where $f^l = \left(f_0^l, \ldots, f_{N-1}^l\right)$ and elements of the $M \times N$ system-object matrix $\boldsymbol{A}^l$ are

$$a_{m,n}^l = \Phi(\boldsymbol{k}(t_m))\, e^{-j\Delta\omega_n^l t_m} e^{-j2\pi(\boldsymbol{k}(t_m)\cdot\boldsymbol{r}_n)}. \quad (4)$$

To estimate the unknown object slice $\boldsymbol{f}^l$ from the observed k-space data, the iterative conjugate gradient algorithm is used to minimize the QPLS cost function

$$\Psi_1\left(\boldsymbol{f}^l\right) = \|\boldsymbol{u}^l - \boldsymbol{A}^l \boldsymbol{f}^l\|^2 + \beta\|\boldsymbol{C}\boldsymbol{f}^l\|^2 \quad (5)$$

where $\boldsymbol{C}$ is a first-order difference matrix, and β is a parameter that controls the tradeoff between obtaining a data-consistent estimate and a smoothed, regularized estimate. The QPLS estimate of $\boldsymbol{f}^l$ is

$$\hat{\mathbf{f}}_{QPLS}^l = \underset{f}{arg\,min}\, \Psi_1(\mathbf{f}) = \left[\mathbf{A}^{l*}\mathbf{A}^l - \beta\mathbf{C}^*\mathbf{C}\right]^{-1}\mathbf{A}^{l*}\mathbf{u}^l, \quad (6)$$

where an asterisk denotes a matrix complex conjugate transpose operation. However, we minimize Eq. (5) using the conjugate gradient algorithm instead of evaluating Eq. (6) directly.

To accurately perform field-corrected reconstruction in the presence of head motion, every slice of observed data $\boldsymbol{u}^l$ should be paired with a dynamic field-map slice $\Delta\omega^l$ that describes the field-inhomogeneity at frame l of the fMRI experiment. Typically, however, only a static field-map $\Delta\omega_{\text{static}}$ is available. This field-map is usually acquired before or after the experiment and does not track field-inhomogeneity changes during the acquisition of the fMRI time series images. Each volume in the EPI time series typically has a lower spatial resolution and larger slice thickness than $\Delta\omega static$. A simple approach to obtain field-corrected fMRI images is to register each time series volume to the image intensity volume acquired in the same coordinate space as the static field-map volume, and then use re-sampled slices of $\Delta\omega static$ in place of $\Delta\omega^l$ in minimizing Eq. (5). This correction method ignores inter-slice motion and field-inhomogeneity changes due to head motion and thus yields potentially significant image reconstruction errors.

2.3 Map Slice-To-Volume (MSV) Registration

The MSV motion correction technique [12] models the 3D motion of multislice EPI data by allowing each slice to have its own six degrees of freedom motion. In MSV, each reconstructed EPI slice $\boldsymbol{f}^l$ is registered with a 3D reference volume $\boldsymbol{g}_{ref}$ using the six degrees of freedom rigid body transform denoted by $T_{\alpha l}$. The vector $\boldsymbol{\alpha}^l$ consists of the six MSV motion parameters t_x, t_y, t_z, θ_x, θ_y, θ_z for slice l. This is performed by minimizing a function $\Psi_2(\boldsymbol{\alpha}^l)$ that measures the dissimilarity between $\boldsymbol{f}^l$ and $\boldsymbol{g}_{ref}$. In the implementation of MSV, the negated mutual information (MI) is used, which performs well for multi-modality datasets, i.e. $T_2{}^*$-weighted EPI slices registered with a T_1-weighted reference volume. The motion parameters $\boldsymbol{\alpha}^l$ are estimated by minimizing the following cost function over $\boldsymbol{\alpha}^l$ using the Nelder-Mead downhill simplex optimization algorithm

$$\Psi_2\left(\boldsymbol{\alpha}^l\right) = -\,MI\left(\boldsymbol{g}_{ref}, \boldsymbol{f}^l\left(T_{\boldsymbol{\alpha}^l}\left(\boldsymbol{r}\right)\right)\right) \quad (7)$$

Each set of optimized motion parameters is then used to transform and interpolate (trilinear) its respective slice $\boldsymbol{f}^l$ into a volume with the same spatial coordinates as the reference volume. In the original MSV method, the motion of each slice is computed independent of other slices and allows six degrees of freedom between each slice acquisition. For single shot acquisition, intra-slice motion is negligible. Given that head motion is typically correlated in time and that MSV may generate outlier estimates, especially for top slices where the information content is reduced, we apply temporal median filtering on the recovered MSV motion parameters before use. A median filter was chosen because the MSV motion estimates obtained from data with simulated smooth motion were observed to track the ground truth except for intermittent outlier estimates. It is noted that median filtered MSV motion parameters are used to compute field map updates in the concurrent field-map MSV (CFMMSV) method and not for repositioning EPI slices into the anatomical reference volume, i.e. EPI motion correction. The latter is done with raw unfiltered MSV motion parameters.

3. Materials and Methods

All experiments were performed on Intel Pentium 4 Xeon 3.0GHz CPUs using MATLAB (The Mathworks Inc., Natick, MA, USA) and Advanced Visual Systems (Advanced Visual Systems Inc., Waltham, MA, USA).

3.1 Concurrent Field-inhomogeneity Correction with MSV

To design a concurrent correction technique that involves Eqs. [5] and [7] with a rigid body transformation function, the main challenge is the approximation of the dynamic field-map from the initial static field-map. To partially account for field-map changes due to 3D head motion during the fMRI experiment, we propose and evaluate the following "concurrent" correction approach. The concurrent field-map and MSV motion correction framework (CFMMSV) loops through several correction cycles, each of which consists of a field-corrected reconstruction stage followed by MSV registration. The changing field-map is approximated using the recovered MSV motion estimates and the static field-map. As the number of correction cycles increases, the geometric distortion is incrementally corrected in the image reconstruction stage. Thus, a rigid body transformation function in MSV is expected to be sufficient to correct for head motion. This leads to a faster image registration process compared to the use of 3D non-linear warping functions.

Since the true dynamic field-map $\Delta\omega^l$ in Eq. (4) is unavailable, the EPI time series image reconstruction in the *initial cycle* ($\kappa = 0$) of the concurrent correction algorithm is performed with the static field-map volume $\Delta\omega_{\text{static}}$. The elements of the system matrix $\boldsymbol{A}^{l,\kappa=0}$ can be written as

$$a_{m,n}^{l,\kappa=0} = \Phi\left(\boldsymbol{k}\left(t_m\right)\right) e^{-j\Delta\omega_{n,static}^{l} t_m} e^{-j2\pi\left(\boldsymbol{k}(t_m)\cdot\boldsymbol{r}_n\right)} \quad (8)$$

where κ denotes the correction cycle number. The first field-corrected estimate of slice frame l, $\hat{\boldsymbol{f}}^{l,\kappa=0}$, is then obtained by minimizing Eq. (5) with $\boldsymbol{A}^l = \boldsymbol{A}^{l,\kappa=0}$. The reconstructed slices are then registered via MSV to the reference volume $\boldsymbol{g}_{\text{ref}}$ by minimizing Eq. (7). Each set of median filtered motion parameters $\hat{\boldsymbol{\alpha}}_{filt}^{l,\kappa}$, $l = 0,..,L\text{-}1$, is applied to the original static field-map volume and the respective slice within the transformed field-map volume is re-sampled and stacked into a new field-map volume

$$\Delta\hat{\omega}^{l,\kappa+1} = H^l\left\{\omega_{static}\left(T_{\hat{\boldsymbol{\alpha}}^{l,\kappa}}\left(\boldsymbol{r}\right)\right)\right\}, \quad l = 0,..,L-1, \quad (9)$$

where $H^l\{U\}$ denotes an operator which re-samples slice l from a volume U. This updated field-map is then used in the next cycle to reconstruct field-corrected images again from the original k-space data.

Since geometric distortion in EPI is predominantly in the phase encoding direction, the recovered MSV motion parameters in the phase encoding direction are *not* used to transform the static field-map in the initial field-map update when $\kappa = 0$. This is because the EPI image shifts in the phase encoding direction may be largely influenced by field-inhomogeneity induced geometric distortion rather than object motion. This is illustrated in the MSV

estimates of translations in the phase encoding direction (Fig. 1) for a simulated EPI time series (Dataset A) with applied motion in three translational directions and in-plane rotation about the *z* axis. In Fig. 1, field-inhomogeneity induced geometric distortion in the phase encoding direction cause significant MSV errors for the distorted EPI data as well as the field-corrected EPI data in cycle 0 (κ=0). Correction cycles 1 to 3 yield estimates of t_y that are close to the ground truth. In addition to translation in the phase encoding direction, the field-map may change significantly with out-of-plane rotations which would render these motion parameters unreliable for the initial field-map update. Thus, for $\kappa = 0$, the motion parameters t_y (translation in phase encoding direction), θ_x and θ_y (out-of-plane rotations) are omitted when applying the transformation $T_{\hat{\boldsymbol{\alpha}}^{l,\kappa=0}}$ to the static field-map. For the following cycles, $\kappa \geq 1$, all six degrees of freedom are used when applying $T_{\hat{\boldsymbol{\alpha}}^{l,\kappa}}$ to update the field-map. The original raw data $\boldsymbol{u}$ and static field-map $\Delta\omega static$ are used in each cycle to approximate the dynamic field-map and field-corrected EPI images to avoid error propagation due to intermediate processing steps as the number of cycles increases. The CFMMSV method is summarized as follows:

Algorithm. Concurrent QPLS-MSV for EPI Motion and Field-Inhomogeneity Correction

---

Initial data: $\Delta\hat{\omega}^{l,\kappa=0}$ *(slice l of static field-map* $\Delta\omega_{static}$*),* u^l *(k-space data), l=0...L-1*

for κ*=0...K (correction cycles)*

Step 1: $\hat{f}^{l,\kappa} = \arg\min_f \| u^l - A(\Delta\hat{\omega}^{l,\kappa}) f \|^2 + \beta \| Cf \|^2$ *do for l=0...L-1 (**QPLS**)*

Step 2: $\hat{\boldsymbol{\alpha}}^{l,\kappa} = \arg\min_{\boldsymbol{\alpha}} \{ -MI(g_{ref}(r), \hat{f}^{l,\kappa}(T_{\boldsymbol{\alpha}}(r))\}$ *do for l=0...L-1 (**MSV**)*

Step 3: Median filter $\hat{\boldsymbol{\alpha}}^{\kappa}$ *to obtain* $\hat{\boldsymbol{\alpha}}^{\kappa}_{filt}$.

Step 4: $\Delta\hat{\omega}^{l,\kappa+1} = H^l \{ \Delta\omega_{static}(T_{\hat{\boldsymbol{\alpha}}^{\kappa}_{filt}}(r)) \}$ *do for l=0...L-1 (**resample slice l**)*

end

The computation times for field corrected iterative reconstruction and MSV is 1.5 mins/ slice and 3 mins/ slice, respectively.

3.2 Motion, Functional Activation and Geometric Distortion Simulation in EPI Time Series

To evaluate the effectiveness of the CFMMSV method in recovering accurate motion parameters, forming accurate field-corrected intensity images and detecting functional activation regions, two time series datasets, labeled A and B, were simulated with different applied motion. The ground truths available for head motion, activation regions and non-distorted image intensities enable quantitative evaluation of the correction method. We started with two perfectly registered T_1- and T_2-weighted image datasets (matrix size: 256×256×124, voxel size: 0.8mm×0.8mm×1.5mm) derived from International Consortium of Brain Mapping (ICBM) data. The T_1 volume served as the anatomical reference for MSV registration and the T_2 volume was the “baseline” volume from which the time series datasets were simulated. The spatial coordinates *x*, *y* and *z* for each volume denote in-plane

image column (sagittal planes), in-plane image row (coronal planes) and through-plane slice (axial planes) directions, respectively. A rotation about a given axis denotes a rotation about the center of the volume perpendicular to that axis. To simulate functional activation, an "activated" T_2 volume was created by increasing the T_2 ICBM dataset intensity by 5% in pre-defined ellipsoidal regions as shown in Figs. 8E and 8J. Six baseline-activation cycles, each of which was formed by concatenating ten baseline and ten activated T_2 volumes, were assembled to form a 120-volume time series. In addition, a simulated brain static field-map was created by adding three 3D Gaussian blobs located at the inferior frontal and temporal lobes to a 3D third-order polynomial (Fig. 2). This field-map was scaled such that the off-resonance values range from -64 Hz to +320 Hz to simulate a maximum field-inhomogeneity of 5 ppm at 1.5 T.

Dataset A is a geometrically distorted EPI time series with simulated motion in t_x, t_y, t_z and θ_z (translations and in-plane rotation) while dataset B is a geometrically distorted EPI time series with simulated motion in θ_x, θ_y and θ_z (rotations). To generate dataset A, temporally smooth translational and in-plane rotational motion (t_x, t_y, t_z and θ_z) were applied to both the T_2-weighted baseline-activation time series and simulated field-map volumes. Sequential 5.6 mm thick slices were then re-sampled to form 120-volume intensity and field-map time series datasets (volume matrix size: 128×128×14). Each re-sampled slice has its own set of motion parameters. The applied motion has maximum values of 7.20 mm, 8.00 mm, 3.51 mm and 4.70° for t_x, t_y, t_z and θ_z, respectively. The T_2-weighted volumes obtained are henceforth referred to as the time series image intensity ground truth without geometric distortion. These were used to compute the image normalized root mean square error (RMSE) values at various correction cycles to measure the accuracy of the field-corrected reconstructed images. The applied motion did not change the orientation of the air-tissue interface with respect to B_0 and thus is unlikely to change the field-map significantly except for the respective translation or in-plane rotation. Thus, forward distorting the T_2 volume with the rotated-translated field-map is reasonable as long as out-of-plane rotations θ_x and θ_y are not applied. However, to test the effectiveness of the CFMMSV framework in the presence of out-of-plane motion while assuming the field-map moves with a rigid body transformation function together with the head, a second pair of 120-volume time series intensity and field-map datasets (dataset B) were simulated with temporally smooth motion in three rotation parameters θ_x, θ_y and θ_z. The assumption that the static field map moves with the head, while simplistic in the presence of large out-of-plane motion, provides a way to generate an otherwise realistic time series dataset with out-of-plane motion and subsequent field-inhomogeneity induced geometric distortion. Datasets A and B are not meant to be compared with each other. They illustrate the performance of the algorithm for different types of applied motion, not for different types of motion-induced field map changes. The simulated rotational motion has maximum values of 5.0°, 8.6° and 8.1° for θ_x, θ_y and θ_z respectively. Slice acquisition interleaving was incorporated when generating both time series datasets.

To forward distort the T_2 time series images from both datasets, simulated blipped EPI Cartesian *k*-space data of the distorted images were generated in conjunction with the respective field-map time series with motion using Eq. (1). The distorted images (Fig. 3B)

were then reconstructed from this *k*-space data using a system model with a field-map set to zero [16]. The simulated readout time was 43.8 ms and the pixel bandwidth in the phase encoding direction was 22.8 Hz. In subsequent sections, datasets A and B will refer to the final *geometrically distorted* time series with the respective applied motion.

3.3 Activation Detection with Random Permutation Test

After re-positioning all the EPI time series slices into volumes, MSV yields time series volumes that may have empty voxels. This results in variable sample sizes for different voxels for statistical analysis. The non-parametric statistical method of voxel-wise random permutation, using the averaged difference between activation and rest images as the test statistic, was used for significance testing of differences in voxel intensities in the simulated datasets [12,21]. This statistical technique is simple, robust and independent of sample size variability [22]. Random draws of 2000 permutations of activated and rest periods were used to form a permutation distribution for each voxel from which activated regions are identified by testing the null hypothesis of no activation at a fixed threshold of P = 0.001. To obtain ROC curves, we vary the threshold a values from 10^{-4} to 1.0 to obtain a set of activation maps and, together with the ground truth activation map, compute the true positive and false alarm rates. The area under each ROC curve (AUC) is used to measure how accurately the activation regions have been detected.

4. Results

In our experiments, the concurrent correction scheme was evaluated on both simulated EPI time series datasets. Both datasets have known ground truths for the applied slice-wise motion parameters, enabling quantitative evaluation of MSV registration performance. In addition, the non-distorted time series intensity images with applied motion serve as image intensity ground truths to evaluate the performance of the field-corrected image reconstruction process.

We investigated three performances indices. The first two indices, MSV RMSE (Table 1) and image normalized RMSE (Fig. 4), evaluate MSV motion correction and field-corrected reconstruction performance respectively. A final performance index, area under the activation detection ROC curve (Table 3 and Fig. 5), evaluates activation detection accuracy. In Table 1, the MSV RMSE for correction cycle κ for each motion parameter, e.g., translation in *y*, is computed with

$$RMSE\left(t_y,\kappa\right)=\sqrt{\frac{1}{L}\sum_{l=0}^{L-1}\left(\hat{t}_y^{l,\kappa}-t_{y,true}^{l}\right)^2}, \quad (10)$$

where $\hat{t}_y^{\kappa}$ and $t_{y,true}^{l}$ are the estimated and true translation parameters for slice *l*. In Table 2, using translation in *y* as an example again, the standard deviation of the error $e_{ty}^{l,\kappa}=\left(\hat{t}_y^{l,\kappa}-t_{y,true}^{t}\right)$ across all slices in the time series is computed with

$$\sigma_{error}(t_y,\kappa)=\sqrt{\frac{1}{(L-1)}\sum_{l=0}^{L-1}\left(e_{ty}^{l,\kappa}-\bar{e}_{ty}^{\kappa}\right)^2}, \quad (11)$$

where $\bar{e}_{ty}^{\kappa}$ is the mean registration error of t_y across all slices.

Tables 1 and 2 list the MSV RMSE and error standard deviation values of the estimated MSV motion parameters. With median filtering of the estimated MSV parameters, the errors decrease as κ increases and empirically converge to relatively small values. This implies that registration accuracy has improved with the concurrent correction method compared to a single-cycle correction method where a static field-map is used for geometric distortion correction prior to MSV (cycle 0). The observed empirical convergence strongly suggests that the algorithm is relatively stable as κ increases.

In fMRI, the accuracy of the reconstructed images' intensity values is of key importance since brain activation maps are computed from the change in image intensity values in the time-series. To measure image quality, the normalized root mean square error values between corrected EPI slices and their corresponding T_2-weighted ground truth images were computed and averaged over the 120 volumes. Fig. 4 shows that the average normalized RMSE of each slice in the 14-slice T_2-weighted volume decreases as κ increases. Empirical truth images were computed by correcting the simulated EPI time series images with the exact same dynamic field-map that was used to distort them. The empirical truth images contain errors inherent to the image reconstruction and MSV processes and represent the best images that can be obtained using these correction methods if the simulated dynamic field-map were known exactly. These empirical ground truth images are *not* the known ground truth intensity images that subsequently corrected datasets are compared to in computing the image intensity normalized RMSE values. It is observed that when $\kappa \geq 2$, the corresponding normalized RMSE values converge to the normalized RMSE values of the empirical truth images which implies that the CFMMSV method yielded updated field-maps that are very close to the ground truth dynamic field-maps. Fig. 6 shows reconstructed EPI slices from the same position in the head and their corresponding absolute error images when compared to corresponding T_2-weighted ground truth images as κ increases. The field-corrected image errors are greatly reduced when $\kappa \geq 3$.

As κ increases, the field-corrected EPI images become more similar to the ground truth T_2 images. However, it is possible to reduce image normalized RMSE without improving activation detection because the simulated intensity increase is only 5% and applied to a relatively small subset of activated voxels. Thus, we applied the statistical random permutation test on datasets A and B at all stages of the CFMMSV correction process and computed ROC curves and respective AUC values to verify that activation detection performance improves as κ increases. Figs. 5A-B show the ROC curves for both datasets at several stages of the CFMMSV correction process and Table 3 shows the corresponding AUC values. For both datasets, the AUC values increase significantly between cycle 0, which are the results one would obtain if the same static field-map was used to correct all the time series data, and cycle 3, which are the final results after applying the CFMMSV

method. The improvement in activation detection is even more significant upon considering that fMRI statistics are often computed directly from EPI datasets without geometric distortion correction, i.e., compare the AUC values between the distorted dataset and cycle 3. Fig. 7 shows the activation maps obtained (P = 0.001) for two slices from datasets A and B at several stages in the CFMMSV correction process. Comparing the activation maps for cycle 0 (second row) and cycle 3 datasets (third row), we see that the latter has more true positives and fewer false positives. The ground truth activation regions for the two slices are shown in Figs. 7E and 7J. Activation maps obtained by applying the random permutation test on the ground truth time series images for both datasets are also shown (fourth row) to illustrate the best performance obtainable with the statistical analysis method used.

5. Discussion

The proposed CMFMSV framework is a retrospective correction framework that incorporates slice-to-volume registration, field-map updating and geometric distortion correction for the purpose of improving activation detection performance in fMRI. In this work, we performed iterative field-corrected reconstruction to remove geometric distortion and employed a field-map updating scheme that applies rigid body MSV motion parameters to a high resolution static field-map of the object. Our results on two simulated EPI time series datasets show that as the number of correction cycles increases, the field-corrected image quality and the accuracy of recovered MSV motion parameters improve and empirically converge to the ground truths. This is evident in the decreasing MSV RMSE, MSV error standard deviation and image normalized RMSE values as κ increases (Tables 1 and 2 and Fig. 4). Improved activation detection performance, as inferred from the increasing AUC values in Table 3, is also observed as κ increases. These results demonstrate that, under the simulated conditions, the CFMMSV method can provide effective correction of motion artifacts that are complicated by the field effects induced by rigid head motion. It is interesting to note that for dataset A, the AUC value for cycle 0 actually decreased when compared to the AUC value for the distorted dataset. The AUC values increased subsequently in cycles 1 through 3. This illustrates that in the presence of significant motion, using a static field-map to correct an entire time series can lead to degraded activation detection performance, even after applying motion correction to the time series data. This is because *all* motion-induced field-map changes were ignored in cycle 0.

Some outlier MSV motion estimates in the time series may result from local minimum solutions obtained by the Nelder-Mead implementation of the mutual information-based registration algorithm. This occurs infrequently and is likely due to the inherent reduced information content of slice-to-volume registration. Using a median filter on the motion estimates for the purpose of updating the field map is akin to throwing out wrong estimates and “interpolating” a value to replace them, given the prior assumption that head motion is correlated in time. Since the goal in fMRI is activation detection accuracy and not necessarily perfect motion correction accuracy, it is conceivable that an alternative, and perhaps conventional, approach to handle outlier estimates in slice-wise registration, e.g., topmost slices of the brain where information content is greatly reduced, is to just exclude those slices from statistical analysis for activation detection. That is a common statistical data analysis approach when outliers are present (data cleaning). However, this would mean

fewer temporal samples available for statistical analysis for each voxel. Temporal filtering (median filter in our case) attempts to retain these outlier slices for statistical analysis for activation detection. In all likelihood, a better approach to remove such outliers exists, and is a subject for future work.

In the first concurrent correction cycle, i.e., $\kappa=0$, the estimated translations in *y* were not used to update the field map since t_y includes geometric distortion effects in addition to spatial motion in *y* by the object. It might be argued that rotations in *z* should also be ignored since they give rise to in-plane translation components. However, θ_z does not need to be omitted in the field map update process when $\kappa=0$ because after the registration is done in MSV, rotations are computed (relatively accurately) from the final control points before the translations are estimated. If estimates of θ_z are omitted in the zeroth iteration, the algorithm is unnecessarily deprived of a piece of relatively accurate information for improving the next field map estimate.

Dataset A was simulated with relatively realistic assumptions of how the susceptibility-induced field-map changes with translations and in-plane rotation. Thus, the results obtained from that dataset are a reasonable indication of the performance of the concurrent correction method on well-shimmed real MR data with such motion. For real MR data, the field-map may include other contributions like post-shim system-induced field-inhomogeneity that remain stationary with respect to the head. Since the focus of the simulation study is on susceptibility-induced artifacts, we have assumed that these additional field-map contributions are less dominant and can be characterized separately, if necessary. This is a reasonable assumption for data collected from a well-shimmed magnet. Dataset B was simulated with similar assumptions as dataset A except that *local* field-map changes that may arise due to out-of-plane rotations are not modeled exactly. Thus, the results from dataset B are less indicative of the CFMMSV method's performance on real MR data in the presence of larger out-of-plane rotation. However, for small out-of-plane motion, the local field-map changes may be small enough [6] to justify the assumption that the dynamic field-map can be approximated with a rigid-body transformation of the static field-map.

For time series datasets that do not have ground truths, an appropriate stopping criterion is necessary to terminate the CFMMSV correction process automatically. In Table 1 and Fig. 4, respectively, the MSV RMSE and image normalized RMSE values remain relatively constant for $\kappa \geq 2$ for both datasets A and B which suggests that the procedure could be terminated earlier, thus reducing computation time. However, the increasing AUC values in Table 3 indicate that activation detection performance continues to improve for $\kappa \geq 2$. Thus, there is a computation time versus activation detection performance tradeoff that may influence the choice for the stopping criterion. To obtain minimal computation time at the expense of activation detection performance, the CFMMSV process can be automatically terminated when the time series' average normalized RMSE difference for the previous two cycles are below a threshold value. For maximal activation detection performance, the number of non-overlapping activated voxels for the previous two cycles can be used as a dissimilarity measure to automatically stop the CFMMSV process.

The iterative field-corrected reconstruction technique corrects for geometric distortion in both the phase encoding and read-out directions if the field map is accurate. Initially, the field map is not accurate as it does not track head motion. In the field-map update process in cycle 0 (κ=0), we use the prior knowledge that the phase encoding distortion is larger than the read-out distortion to avoid using the phase encoding direction MSV motion parameter (t_y) to update the field-map. Subsequently, as the updated field maps become more aligned to the true field map (i.e., more accurate field map is obtained), the iterative field-corrected reconstruction algorithm corrects for both phase encoding and read-out geometric distortions more accurately.

The CFMMSV framework was formulated to jointly correct for motion and geometric distortions arising from susceptibility-induced field-inhomogeneity without the explicit acquisition of dynamic field-maps. The framework can be further improved by using field-map update techniques that account for susceptibility-induced field-map changes with out-of-plane rotation. For example, a conceivable modification would be to apply MSV motion parameters to a high resolution 3D volume of a brain that has been segmented into air, bone and soft tissue regions. The susceptibility-induced component of the dynamic field-map can then be re-estimated from the transformed 3D structural volume using numerical techniques to approximate solutions to the magnetostatic scalar potential based on Maxwell's equations [23,24]. This will increase the computational cost but may yield improved performance. Future work includes a susceptibility phantom study of the robustness of CFMMSV with out-of-plane rotations.

We have focused this study as a validation work using truths available in the simulation data. While it is the ultimate goal of the continued investigation, studies dealing with human fMRI data would pose additional problems that may complicate the validation process. The lack of known truths would be the primary cause of difficulty in the evaluation. Other intricacies involving human data analyses would be brief real motion, such as jerking or swallowing and the extent of motion that can be corrected. In real subject motion, transient motion spikes are often present due to brief motions followed by return to baseline (e.g., swallowing). Modeling of such spikes was not included in this study. However, characterization and implementation of better matching filtering would be more practical with the future studies with human data. The extent of motion that can be corrected by CFMMSV can be explored with real MR data using a susceptibility phantom.

6. Conclusions

A proposed technique to perform concurrent susceptibility-induced geometric distortion correction with slice-to-volume motion correction for EPI fMRI data has been evaluated on two 120-volume simulated time series with different applied motion. Under the simulated conditions, the CFMMSV method improved the accuracy in recovering both the MSV motion parameters and the field-corrected reconstructed images compared to the simpler method of performing motion and geometric distortion correction independently. Activation detection performance, quantified using the AUC values at various stages in the CFMMSV correction process, also improved with the CFMMSV method. Although the CFMMSV method may currently be limited to small out-of-plane rotations, it presents a correction

framework that addresses geometric distortion and slice-wise head motion as a joint problem and has the potential to perform better than methods that ignore the relationship between these two problems.

Acknowledgments

This work was supported in part by the National Institute of Health grant 1P01 CA87634 & R01 EB00309.

References

1. Friston KJ, Ashburner J, Frith CD, Poline JB, Heather JD, Frackowiak RSJ. Spatial registration and normalization of Images. Hum Brain Map. 1995; 2:165–189.
2. Bullmore E, Brammer M, Williams SCR, Rabe-Hesketh S, Janot N, David A, Meller J, Howard R, Sham P. Statistical methods and estimation and inference for functional MR image analysis. Magn Reson Med. 1996; 35:261–277. [PubMed: 8622592]
3. Hu X, Le TH, Parrish T, Erhard P. Retrospective estimation and correction of physiological fluctuation in functional MRI. Magn Reson Med. 1995; 34:201–212. [PubMed: 7476079]
4. Hajnal JV, Myers R, Oatridge A, Schwieso JE, Young IR, Bydder GM. Artifacts due to stimulus correlated motion in functional imaging of the brain. Magn Reson Med. 1994; 31:283–291. [PubMed: 8057799]
5. Andersson JLR, Hutton C, Ashburner J, Turner R, Friston K. Modeling geometric deformations in EPI time series. Neuroimage. 2001; 13:903–919. [PubMed: 11304086]
6. Jezzard P, Clare S. Sources of distortion in functional MRI data. Human Brain Mapping. 1999; 8:80–85. [PubMed: 10524596]
7. Cusack R, Brett M, Osswald K. An evaluation of the use of magnetic field maps to undistort echo-planar images. Neuroimage. 2003; 18:127–142. [PubMed: 12507450]
8. Roopchansingh V, Cox RW, Jesmanowicz A, Ward BD, Hyde JS. Single-shot magnetic field mapping embedded in echo-planar time-course imaging. Magn Reson Med. 2003; 50:839–843. [PubMed: 14523971]
9. Sutton BP, Noll DC, Fessler JA. Dynamic field map estimation using a spiral-in/spiral-out acquisition. Magn Reson Med. 2004; 51:1194–1204. [PubMed: 15170840]
10. Andersson JLR, Skare S, Ashburner J. How to correct susceptibility distortions in spin-echo echo-planar images: application to diffusion tensor imaging. Neuroimage. 2003; 20:870–888. [PubMed: 14568458]
11. Chang H, Fitzpatrick JM. A technique for accurate magnetic resonance imaging in the presence of field inhomogeneities. IEEE Trans on Med Imaging. 1992; 11:319–329.
12. Kim B, Boes JL, Bland PH, Chenevert TL, Meyer CR. Motion correction in fMRI via registration of individual slices into an anatomical volume. Magn Reson Med. 1999; 41:964–972. [PubMed: 10332880]
13. Yeo, DTB.; Bhagalia, RR.; Kim, B. Improved map-slice-to-volume motion correction with B0 inhomogeneity correction: Validation of activation detection algorithms using ROC curve analyses.. In: Larsen, R.; Nielsen, M.; Sporring, J., editors. Medical image computing and computer-assisted intervention. Lecture notes in computer science. Vol. 4191. Springer Verlag; 2006. p. 276-283.
14. Kim, B.; Bland, PH.; Meyer, CR. Proceedings of the 7th Annual Meeting of ISMRM. Philadelphia, USA: 2000. Correction of local deformations in fMRI by 3D non-linear warping in map-slice-to-volume approach.; p. 1765
15. Kim, B.; Chenevert, TL.; Meyer, CR. Proceedings of the 10th Annual Meeting of ISMRM. Honolulu, USA: 2002. Motion correction with a non-linear warping solution for activations in temporal region.; p. 2304
16. Yeo, DTB.; Fessler, JA.; Kim, B. Motion correction in fMRI by mapping slice-to-volume with concurrent field-inhomogeneity correction.. In: Barillot, C.; Haynor, DR.; Hellier, P., editors.

Medical image computing and computer-assisted intervention. Lecture notes in computer science. Vol. 3217. Springer Verlag; 2004. p. 752-760.

17. Sutton BP, Noll DC, Fessler JA. Fast, iterative image reconstruction for MRI in the presence of field inhomogeneities. IEEE Trans on Med Imaging. 2003; 22:178–188.
18. Jezzard P, Balaban RS. Correction for geometric distortion in echo planar images from B0 field variations. Magn Reson Med. 1995; 34:65–73. [PubMed: 7674900]
19. Kadah YM, Hu X. Algebraic reconstruction for magnetic resonance imaging under B0 inhomogeneity. IEEE Trans on Med Imaging. 1998; 17:362–370.
20. Haacke, EM.; Brown, RW.; Thomson, MR.; Venkatesan, R. Magnetic resonance imaging: physical principles and sequence design. John Wiley and Sons; New York: 1999.
21. Nichols TE, Holmes AP. Nonparametric permutation tests for functional neuroimaging: A primer with examples. Hum Brain Map. 2002; 15:1–25.
22. Good, P. Permutation tests. Springer-Verlag; New York: 1994.
23. de Munck JC, Bhagwandien R, Muller SH, Verster FC, Van Herk MB. The computation of MR image distortions caused by tissue susceptibility using the boundary element method. IEEE Trans on Med Imaging. 1996; 15:620–627.
24. Truong TK, Clymer BD, Chakeres DW, Schmalbrock P. Three-dimensional numerical simulations of susceptibility-induced magnetic field inhomogeneities in the human head. Magn Reson Imag. 2002; 20:759–770.

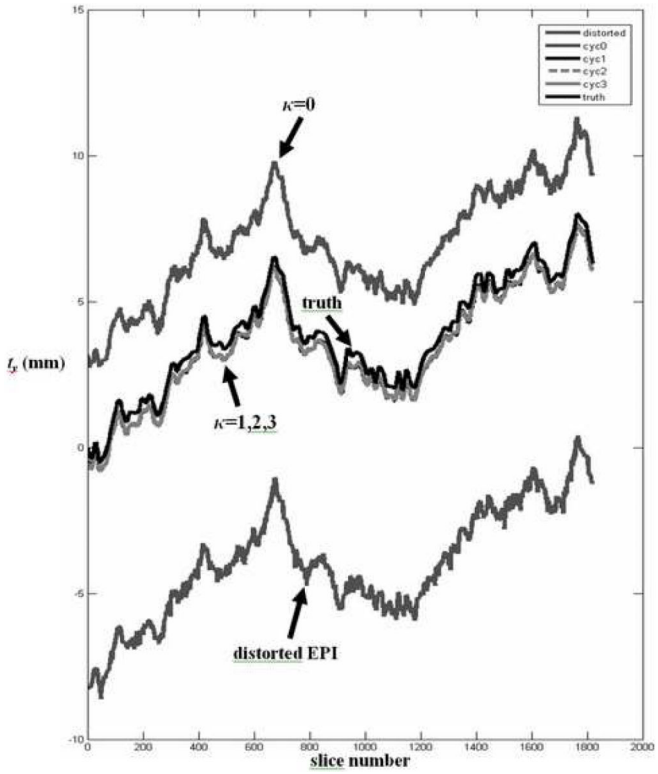

Fig. 1.

Median filtered MSV motion parameter t_y recovered at various correction cycles for dataset A. Field-inhomogeneity induced geometric distortion in the phase encoding direction y cause significant MSV errors for the distorted EPI data as well as the corrected data in cycle 0 (κ=0). Correction cycles 1 to 3 yield estimates of t_y that are close to the ground truth as shown in Tables 1 and 2. The above plot shows 130 simulated volumes instead of the 120 volumes used for subsequent activation analyses.

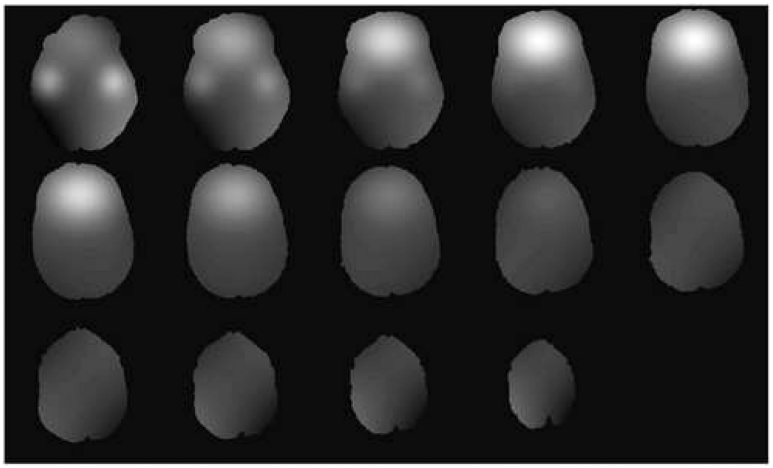

Fig. 2.

Simulated field-map slices from a single volume with significant field-inhomogeneity near frontal lobe and inferior temporal lobe regions. Field-map values range from −64 Hz to +320 Hz to simulate a maximum field-inhomogeneity of 5 ppm at 1.5 T.

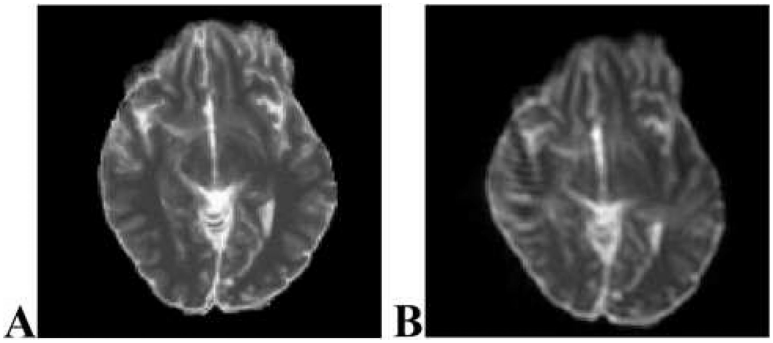

Fig. 3.

(A) T_2 ICBM slice before simulated geometric distortion. (B) T_2 ICBM slice after simulated geometric distortion with a peak field-inhomogeneity of 5 ppm at 1.5 T.

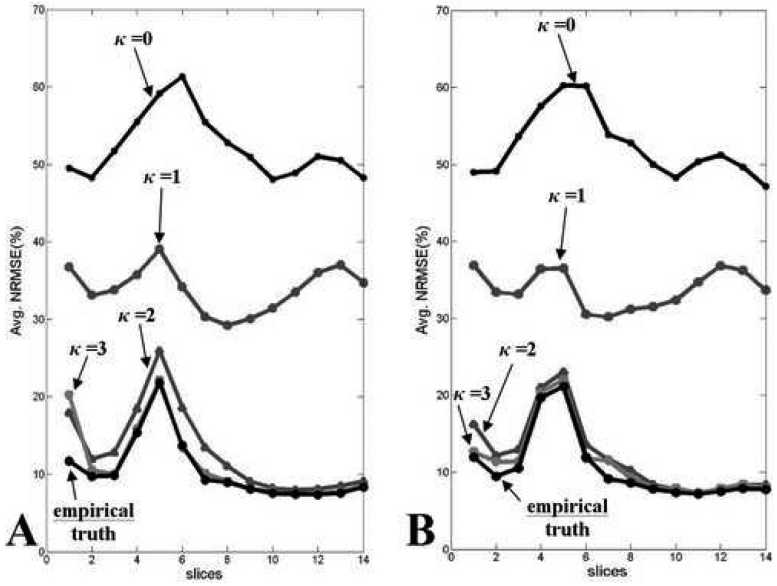

Fig. 4.

Normalized RMSE values for each EPI slice in the same position in the head averaged over 120 volumes for various correction cycles for (A) dataset A with applied t_x, t_y, t_z and θ_z motion, and (B) dataset B with applied θ_x, θ_y, θ_z motion.

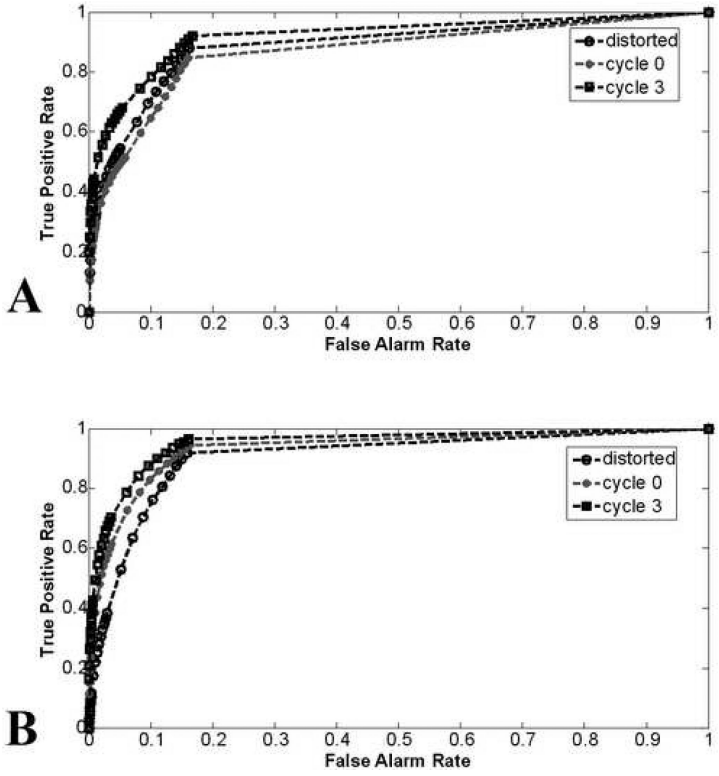

Fig. 5.

ROC curves showing activation detection performance for (A) dataset A and (B) dataset B at several stages in the CFMMSV correction process.

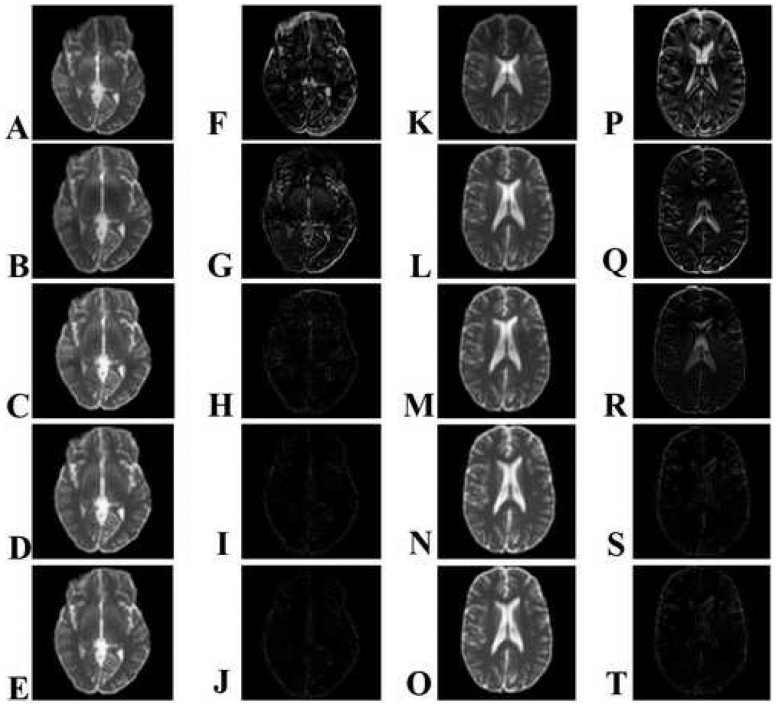

Fig. 6.

(A-E, K-O) Intensity and (F-J, P-T) absolute difference images with respect to ground truth images for two sample slices from dataset A at various stages in the CFMMSV correction process. (Top row) Geometrically distorted dataset, (second row) cycle 0, (third row) cycle 1, (fourth row) cycle 2, (fifth row) cycle 3. All images are displayed on the same normalized intensity scale ranging from 0 to 1.

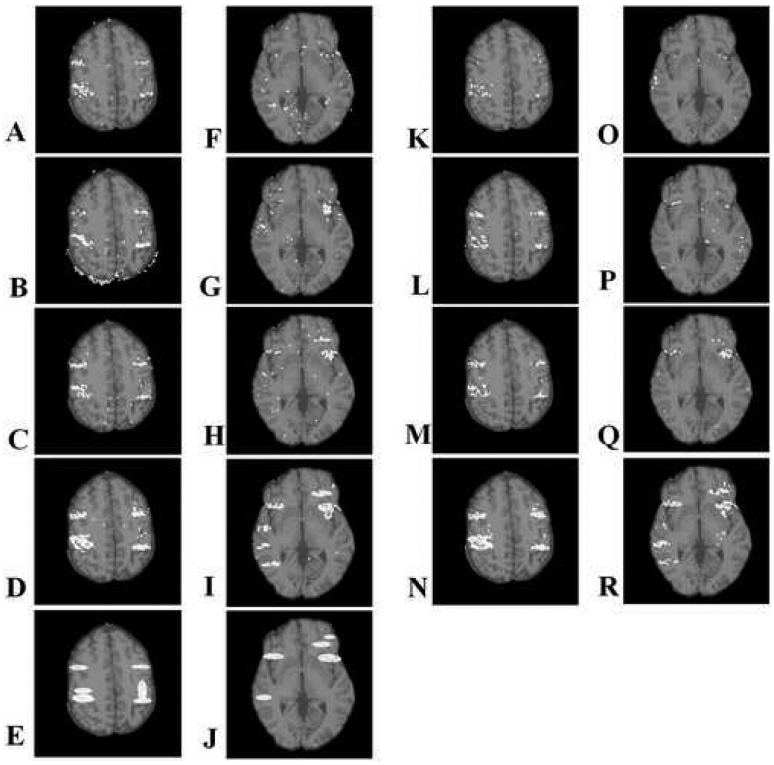

Fig. 7.

Activation detection maps (P=0.001) overlaid on anatomical data of two sample slices from (A-D, F-I) dataset A and (K-R) dataset B at several stages in the CFMMSV correction process. Each row of activation maps corresponds to a specific correction stage consisting of (top row) geometrically distorted, (second row) cycle 0, (third row) cycle 3 and (fourth row) ground truth time series images. The simulated activation maps applied to the two slices are shown in (E) and (J).

Table 1

RMS error of raw MSV estimates for simulated EPI datasets A and B.

Correction cycle	RMSE (mm and °)											
	Dataset A (motion applied: t_x, t_y, t_z and θ_z)						Dataset B (motion applied: θ_x, θ_y, θ_z)					
	t_x	t_y	t_z	θ_x	θ_y	θ_z	t_x	t_y	t_z	θ_x	θ_y	θ_z
Distorted	1.05	8.10	0.96	1.63	1.35	0.92	1.17	7.59	2.52	2.92	1.58	1.04
Cycle 0 (κ=0)	0.57	3.14	0.77	1.69	0.88	0.44	0.42	3.15	0.42	2.91	2.60	0.44
Cycle 1 (κ=1)	0.42	0.54	0.29	0.67	0.30	0.31	0.41	0.43	0.24	0.23	0.24	0.13
Cycle 2 (κ=2)	0.41	0.43	0.29	0.27	0.16	0.09	0.40	0.41	0.23	0.21	0.22	0.10
Cycle 3 (κ=3)	0.44	0.47	0.34	0.27	0.19	0.13	0.40	0.42	0.23	0.22	0.22	0.11

Table 2

Standard deviation of the error of raw MSV estimates for simulated EPI datasets A and B.

Correction cycle	Standard deviation of error of median filtered MSV (mm and °)											
	Dataset A (motion applied: t_x, t_y, t_z and θ_z)						Dataset B (motion applied: θ_x, θ_y, θ_z)					
	t_x	t_y	t_z	θ_x	θ_y	θ_z	t_x	t_y	t_z	θ_x	θ_y	θ_z
Distorted	1.61	15.66	3.45	11.80	11.80	3.26	2.53	20.46	20.53	27.03	11.52	2.21
Cycle 0 (κ=0)	1.77	4.13	3.87	15.31	10.28	0.99	0.25	2.70	2.06	1.71	0.42	0.08
Cycle 1 (k=1)	0.22	2.37	0.24	6.75	1.94	3.10	0.13	0.17	0.10	0.09	0.12	0.03
Cycle 2 (k=2)	0.08	0.50	0.41	1.92	0.09	0.02	0.11	0.15	0.09	0.08	0.08	0.02
Cycle 3 (k=3)	0.34	0.50	0.69	1.47	0.40	0.15	0.11	0.15	0.10	0.09	0.08	0.02

Table 3

Area under ROC curve (AUC) values for activation detection of datasets A and B at various stages in CFMMSV correction.

Correction cycle	Area under ROC Curve (AUC)	
	Dataset A	Dataset B
Distorted	0.8880	0.9043
Cycle 0 (κ=0)	0.8664	0.9295
Cycle 1 (κ=1)	0.8990	0.9382
Cycle 2 (κ=2)	0.9053	0.9519
Cycle 3 (κ=3)	0.9208	0.9521
Ground truth T_2	0.9209	0.9659